Available online at www.sciencedirect.com

ScienceDirect

Acta Materialia 94 (2015) 124–133

Acta MATERIALIA

www.elsevier.com/locate/actamat

Design of a twinning-induced plasticity high entropy alloy

Y. Deng,[a,b] C.C. Tasan,[a,*] K.G. Pradeep,[a,c,*] H. Springer,[a] A. Kostka[a] and D. Raabe[a]

[a] *Max-Planck-Institut für Eisenforschung, Max-Planck-Straße 1, 40237 Düsseldorf, Germany*

[b] *Department of Engineering Design and Materials, Norwegian University of Science and Technology, No-7491 Trondheim, Norway*

[c] *Materials Chemistry, RWTH Aachen University, Kopernikusstr.10, 52074 Aachen, Germany*

Received 13 February 2015; revised 10 April 2015; accepted 10 April 2015

Abstract—We introduce a liquid metallurgy synthesized, non-equiatomic $Fe_{40}Mn_{40}Co_{10}Cr_{10}$ high entropy alloy that is designed to undergo mechanically-induced twinning upon deformation at room temperature. Microstructure characterization, carried out using SEM, TEM and APT shows a homogeneous fcc structured single phase solid solution in the as-cast, hot-rolled and homogenized states. Investigations of the deformation substructures at specific strain levels with electron channeling contrast imaging (ECCI) combined with EBSD reveal a clear change in the deformation mechanisms of the designed alloy starting from dislocation slip to twinning as a function of strain. Such twinning induced plasticity has only been observed under cryogenic conditions in the equiatomic FeMnNiCoCr high entropy alloy. Thus, despite the decreased contribution of solid solution strengthening, the tensile properties of the introduced lean alloy at room temperature are found to be comparable to that of the well-studied five component FeMnNiCoCr system.

Keywords: High entropy alloy; ECCI; EBSD; Lean; Twinning

1. Introduction

In the past decade, the high entropy alloy (HEA) concept has attracted extensive research attention owing to its promising mechanical properties [1–3]. This new alloy design strategy aims at the maximization of the entropy of mixing with the purpose of producing massive solid solution, single phase microstructures. The heavy lattice distortion and the sluggish diffusion introduced as a result of mixing multiple components in equal proportions are proposed to jointly contribute to high thermal stability and good mechanical properties (which can be greatly adjusted by a potential cocktail (multi-phase) effect [4,5]). In order to achieve that, the initially proposed design criterion was based on the presence of at least five elements in equiatomic or near equiatomic concentrations. However, among various HEAs that have been designed according to these criteria (e.g. AlCoCrCuFeNi [6], AlCrFeMnNi [7], FeMnNiCoCr [2,8]), most show multi-phase microstructures and exhibit varied properties (wear resistance, corrosion resistance, high strength, etc). While multiphase HEAs promote fundamental investigations of phase separation in massive solid solutions, and enlarge the achievable property (and hence application) spectrum [9,10], they essentially do not provide proof-of-principle observations for the original concept described above. The only alloy system that develops a single fcc solid solution upon conventional casting is FeMnNiCoCr system. Hence, this most successful example of the HEA concept has been extensively investigated focusing on different aspects such as vacancy motion [11], optimization of mechanical properties by thermo-mechanical treatments [12–14], texture evolution [12] and deformation mechanisms [13].

However, setting the striking stability of the single fcc solid solution aside, the equiatomic FeMnNiCoCr alloy shows significant similarities in terms of mechanical behavior to conventional fcc steels with low stacking fault energy [15,16]. In fact, under quasi-static uniaxial tensile loading, the room temperature mechanical performance of FeMnNiCoCr HEA is well-comparable to those of simple binary Fe–Mn alloys [17]. On the other hand, Gludovatz et al. recently reported that the equiatomic FeMnNiCoCr alloy out-performs all conventional alloys under cryogenic conditions [18]. The fracture toughness values measured by compact tension test at cryogenic temperatures down to 77 k were found to exceed 200 $MPa \cdot m^{1/2}$ at crack initiation and 300 $MPa \cdot m^{1/2}$ for stable crack growth. The underlying deformation mechanism that determines these excellent properties is nanotwinning, which was however not observed at ambient temperatures [13].

Recently, we have shown through non-equiatomic HEA design [14], that the maximization of configurational entropy is not a strict criterion that determines massive solid solution formation, and that it can form over a wide range

* Corresponding authors at. Max-Planck-Institut für Eisenforschung, Max-Planck-Straße 1, 40237 Düsseldorf, Germany.

http://dx.doi.org/10.1016/j.actamat.2015.04.014

of compositions. The reason for this is that the shape of the entropy curve as a function of chemical composition is for most transition metal mixtures very flat so that even larger compositional deviations from the equi-atomic alloying rule yield the same entropy as the an equi-atomic mixing. This thermodynamic relaxation of the originally quite strict high entropy alloy rule opens a wide alloying window for realizing true single phase states and corresponding property tuning. Therefore, composition variations can be explored to optimize the stacking fault energy and to transfer the excellent nanotwinning induced cryogenic mechanical behavior to room temperature. We demonstrate this approach via the design of a lean (i.e. in terms of Co, Cr and especially Ni content with respect to the equiatomic five-component alloy) twinning-induced plasticity high entropy alloy (TWIP-HEA), $Fe_{40}Mn_{40}Co_{10}Cr_{10}$ with excellent room temperature mechanical properties that are comparable to those of advanced TWIP steels [19–22].

2. Methodology

Our alloy design approach is based on the following considerations: As reported elsewhere [23], the stacking fault energy of the equiatomic FeMnNiCoCr alloy was determined to be 25 mJ/m^2 using a combination of density functional theory (DFT) calculations and X-ray diffraction (XRD) experiments. Reducing the Ni content would lower the stacking fault energy and increase the potential applicability of the alloy due to the decreased alloying contents and costs. However, the four component alloy system FeMnCoCr in absence of Ni (i.e. $Fe_{25}Mn_{25}Co_{25}Cr_{25}$) develops a multi-phase microstructure [17,24] with a sigma phase rich in Cr. The Cr rich sigma phase has been reported in several HEA systems such as FeNiCoCr [25] $Co_{0.5}CrFeMn_{1.5}Ni$ [26], $FeNiCoCr_2$ [26], often when Cr is present along with Ni and Co [27]. Our recent observations demonstrate that equi-atomicity is not an essential requirement to ensure a single phase microstructure [14]. Thus, to avoid the sigma phase and achieve a single fcc phase microstructure, we introduce the $Fe_{40}Mn_{40}Co_{10}Cr_{10}$ alloy with reduced Cr and Co content.

In order to verify the validity of this approach, the non-equiatomic $Fe_{40}Mn_{40}Co_{10}Cr_{10}$ alloy was melted in a vacuum induction furnace from metals with purities above 99.8 wt.% and cast into a water-cooled copper mold and allowed for furnace-cooling. Then the material was hot rolled at 900 °C to 50% thickness reduction, followed by homogenization at 1200 °C for 2 h in Ar atmosphere and quenched in water.

The crystal structure of the alloy was analyzed using various techniques. X-ray diffraction measurements (Huber-2 goniometer) were conducted using Co $\kappa\alpha$ radiation ($\lambda = 1.79$ Å). Secondary electron (SE) imaging and electron backscatter diffraction (EBSD) were conducted in a 6500F JEOL field emission gun-scanning electron microscopy (FEG-SEM) equipped with an EDAX software and a TSL OIM EBSD system.

The chemical homogeneity was studied at the microscopic scale using energy-disperse X-ray spectroscopy (EDS), and at atomic scale using local electrode atom probe tomography (APT) (LEAP 3000X HR, Cameca Inc.). To verify the chemical homogeneity in the vicinity of grain boundaries, APT tips were site-specifically produced using focused ion beam (FIB) (FEI Helios Nanolab 600i) from regions including high angle grain boundaries following the procedures described elsewhere [28,29].

Flat dog-bone-shaped tensile specimens with gauge geometry of 10 × 2.5 × 1 mm were machined from the homogenized sheet by electric discharge machining (EDM) with their longitudinal axes perpendicular to the rolling direction of the sheets. Tensile tests were performed at room temperature with a strain rate of 1.0×10^{-3} s^{-1} using a Kammrath and Weiss tensile stage. Prior to tests, both surfaces were polished, a speckle pattern was applied to one of the sides for DIC analysis (Aramis, GOM GmbH; DIC: Digital Image Correlation) while the other side was kept clean for post-mortem trace analysis. During the measurements, the force applied to the sample, the velocity of the movement and the conducting time were recorded, and then the strain and stress were calculated [30–32]. The microstructure after deformation is characterized at different local strain levels using electron channeling contrast imaging (ECCI) technique as well as SE imaging and EBSD. ECCI analysis was conducted using a Zeiss Merlin SEM [33,34].

3. Results

3.1. Microstructure development during processing

Figs. 1 and 2 show the detailed microstructure characterization of the non-equiatomic $Fe_{40}Mn_{40}Co_{10}Cr_{10}$ alloy in the as-cast, hot-rolled and homogenized states.

The XRD patterns, shown in Fig. 1, clearly reveal a single-phase face-centered cubic (fcc) microstructure (lattice parameter = 3.621 Å) in all three processing states. The single phase fcc microstructure was further confirmed by the high resolution EBSD analysis (except for $<\sim 0.4\%$ unindexed points which is attributed to non-indexed interface regions). A large fraction of annealing twins was observed in most of the grains in the homogenized state. The average grain size, measured using linear intercept method, was found to be 108.6 μm (excluding twin boundaries).

The compositional homogeneity of the as-homogenized material was analyzed using EDS and APT as shown in Fig. 2. EDS maps reveal that all elements are homogenously distributed, except for some minor inhomogeneity due to the formation of manganese oxides formed during casting. Several APT tips were lifted out from the grain boundary region as shown in Fig. 2b. The APT results of one of the tips are shown in Fig. 2c. No apparent elemental segregation of the alloying elements (Fe, Mn, Co, Cr) was found in the 3D maps, indicating a random solid solution state in the investigated volume. This is different compared to related FeMn and FeMnNi based alloys which reveal in part substantial Mn segregation at the grain boundaries [35–37]. Furthermore, a binomial frequency distribution analysis was employed to evaluate statistically the random elemental distribution. The binomial curves obtained from the experiments match the curves corresponding to a total random distribution. The quality of the fit was quantified using several parameters, as listed in the insert chart. The normalized homogenization parameter, referred to as μ, ideally ranges from 0 to 1, where 0 refers to total randomness while 1 represents complete ordering [38,39]. For all four alloying elements, the μ values are close to 0, confirming the random distribution of elements in this alloy. The

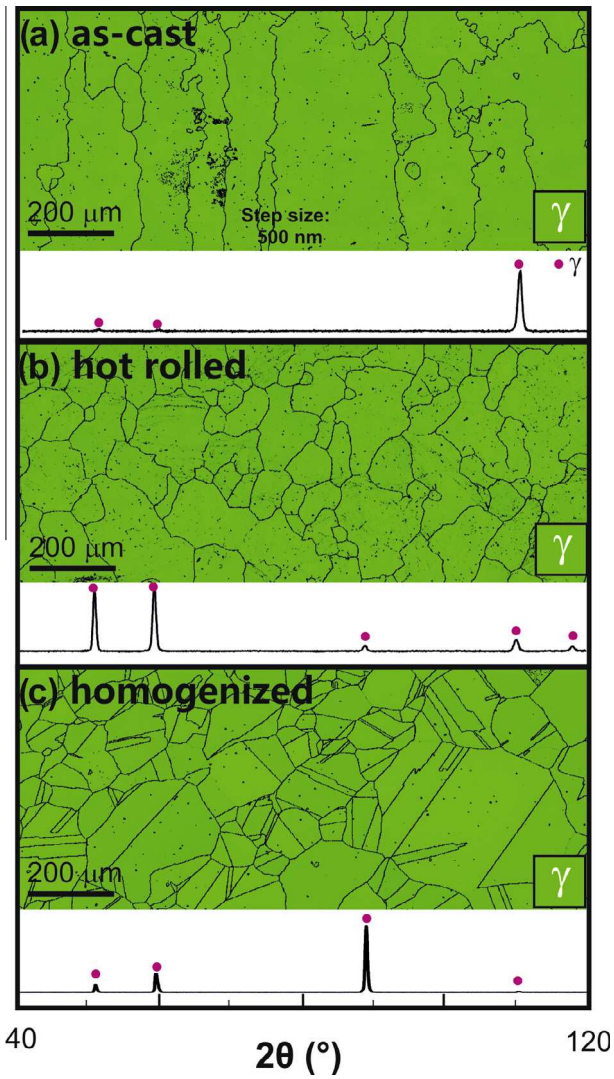

Fig. 1. XRD patterns and EBSD phase maps (using green color for the fcc phase) for the $Fe_{40}Mn_{40}Co_{10}Cr_{10}$ alloy at different process states: (a) as-cast state; (b) hot-rolled state and (c) homogenized state. (For interpretation of the references to color in this figure legend, the reader is referred to the web version of this article.)

concentration of elements across the grain boundary was analyzed within a cylindrical volume ($20 \times 20 \times 60\ nm^3$). The one dimensional concentration-depth profile analysis shows a near uniform distribution for all elements across the grain boundary [40]. The overall bulk concentration of the tip as obtained from APT was $Fe_{42.30}Mn_{36.05}Co_{11.25}Cr_{10.34}$ (all in at.%).

In summary, Figs. 1 and 2 confirm that the single fcc phase in the $Fe_{40}Mn_{40}Co_{10}Cr_{10}$ alloy is stable at different stages of the processing. EDS and APT analyses show excellent homogeneity at the crystal and atomistic scale of the homogenized material. It is thus clear that this lean alloy can reproduce the phase stability and homogeneity reported in the FeMnNiCoCr alloy system [3,8,14].

3.2. Tensile properties

Fig. 3 shows the tensile stress–strain behavior (left) and the hardening curve (right) of the alloy in the homogenized state. The strain hardening curve is calculated as the first derivative of the true stress to the true strain using MATLAB. Despite an expected decrease in solid solution strengthening, and of the larger grain size, the tensile properties of this alloy at room temperature (i.e. yield strength of ~240 MPa, ultimate tensile strength of ~489 MPa and ~58% of total elongation) are found to be comparable to that of the five component equiatomic system $Fe_{20}Mn_{20}Ni_{20}Co_{20}Cr_{20}$ [13] and the previously proposed five component non-equiatomic alloy $Fe_{40}Mn_{26}Ni_{27}Co_5Cr_2$ [14].

The corresponding strain hardening exhibits 3 different regimes, as shown in Fig. 3. Below 4% of the true strain, a continuously decreasing strain hardening rate was observed, between 4% and 25% the rate of decrease of the strain hardening rate decreases and beyond 25% true strain progressive decrease in strain hardening rate can be observed. This strain hardening behavior is similar to that of some TWIP steels [16,20,22].

3.3. Deformation-induced microstructure evolution

Fig. 4 shows the EBSD results obtained for the $Fe_{40}Mn_{40}Co_{10}Cr_{10}$ alloy at different tensile strains. Only fcc phase (green colored area in phase maps) was indexed in all three regions at different strain levels. The high angle grain boundaries and (1 1 1) twin boundaries are marked in the image quality underlayed phase maps in terms of red and blue lines, respectively. At a strain level of 5%, the marked twin boundaries represent annealing twins, and none of the grains shows deformation twins. When the strain level increases to ~10%, mechanically-induced twin boundaries can be indexed (see the blue boundaries inside the grains). The fraction of twin boundaries increases when the deformation level further increases to ~25%. The IPF maps show the grain orientation with respect to the tensile direction. Two major points can be made: (1) No strain induced phase transformation occurs during tensile testing, i.e. only fcc phase is observed in the phase maps at different strain levels. (2) Deformation twinning is activated after ~10% straining and the twin fraction increases with ongoing deformation.

The presence of the deformation twins was further confirmed by TEM analysis, as shown in Fig. 5. The dark field image and the corresponding selected area diffraction (SAD) pattern are shown in Fig. 5. The diffraction pattern provided in Fig. 5b, where the activated twin system was indexed as $[-1\,1\,2](1\,-1\,1)$, analogous to a compound fcc twin commonly observed in fcc crystals [41]. Fig. 5c shows the TEM orientation imaging (ASTAR, NanoMEGAS) map of the same area.

The development of the deformation substructure from 1% up to ~25% was further revealed by ECCI (Fig. 6). At a strain level of ~1%, two sets of piled-up dislocations can be observed (Fig. 6a_1). Upon increasing the strain level to ~5%, the majority of the grains (25 out of 28 analyzed grains in total) reveal a checkerboard-type dislocation pattern, which was created by the intersection of highly dense dislocation walls (HDDWs) on two different slip planes (Fig. 6a_2). This observation suggests pronounced planar slip. Only few grains (3 out of 28 grains) form dislocation cells (DCs), as revealed in Fig. 6a_3, indicating the presence of dislocation multiple slip and cross slip [42,43]. With increasing deformation to ~10% true strain, the majority

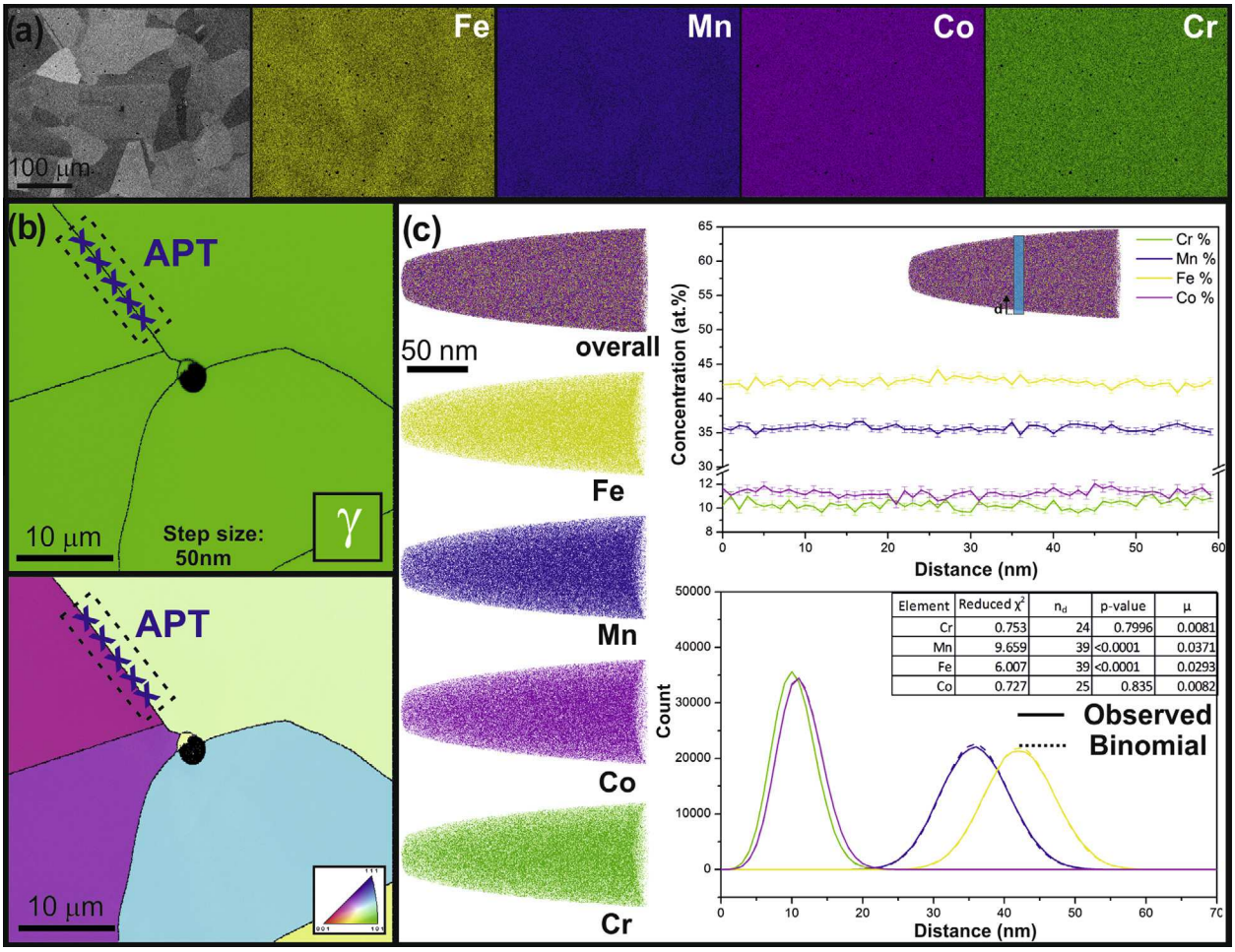

Fig. 2. (a) EDX map showing homogeneous distribution for all elements in the $Fe_{40}Mn_{40}Co_{10}Cr_{10}$ alloy; (b) EBSD phase and IPF maps showing the area for site-specific APT tip preparation (IPF: Inverse Pole Figure); (c) 3D atom maps of all elements and the corresponding 1D concentration profile taken along the cylindrical volume shown in inset and the frequency distribution analyses obtained both from observed experiment results and from binomial simulation.

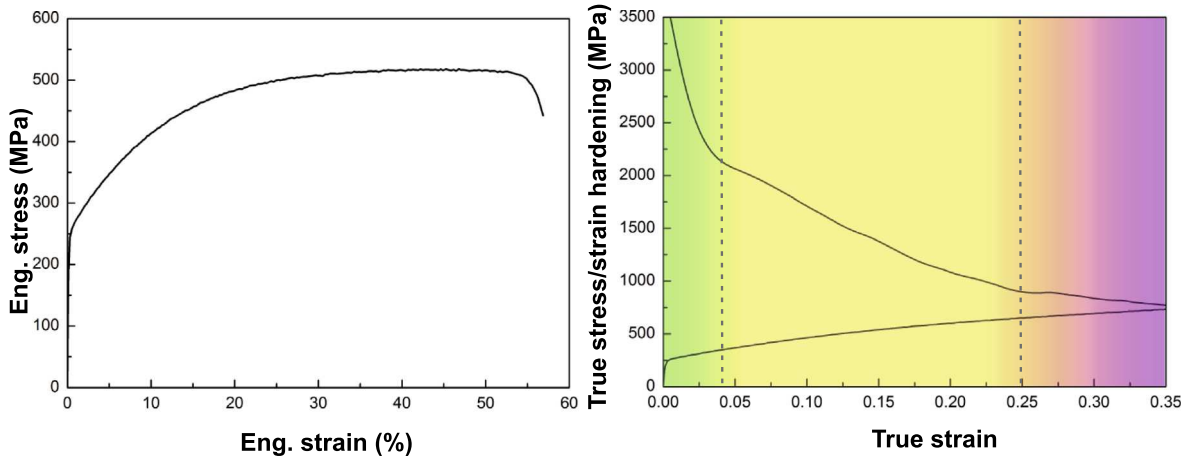

Fig. 3. Room temperature mechanical properties of the newly designed $Fe_{40}Mn_{40}Co_{10}Cr_{10}$ alloy demonstrated in terms of the engineering strain–stress curve (left) and the corresponding strain hardening curve with respect to true strain (right).

of the grains show a pattern of more intense interaction of HDDWs (Fig. 6b_1), and deformation twins appear in some grains (Fig. 6b_2 and b_3). The twins are arranged in bundles, and most of them penetrate the entire grain without much apparent resistance from the dislocation patterns that were formed before. The highly coordinated slip of partial dislocations is proposed to be the possible reason to this unimpeded movement of the twin bundles [20]. However, some

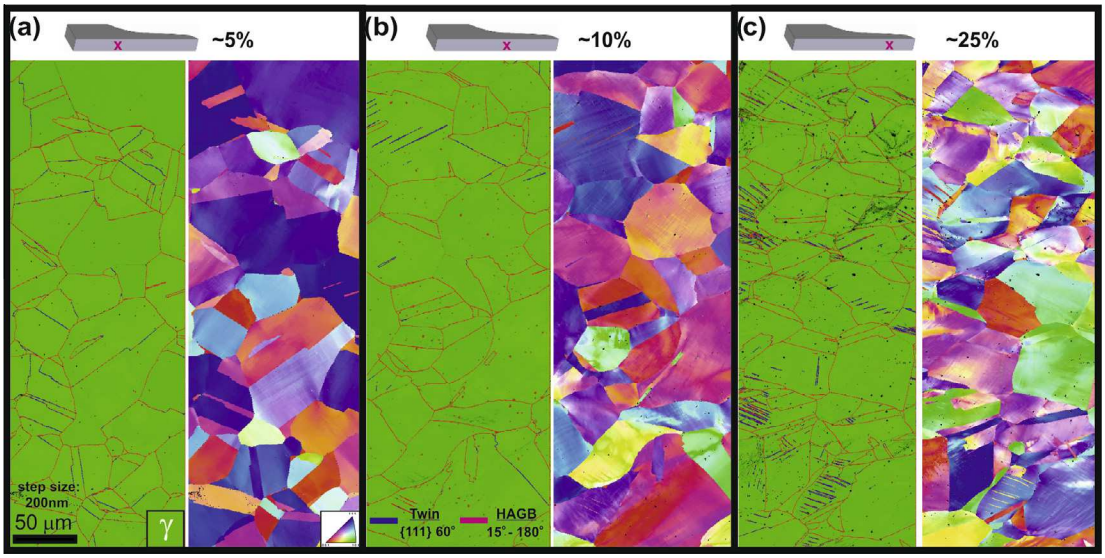

Fig. 4. EBSD phase and IPF maps showing the microstructure at cross section the deformed $Fe_{40}Mn_{40}Co_{10}Cr_{10}$ sample at different stain levels: (a) ~5% strain; (b) ~10% strain; (c) ~25% strain.

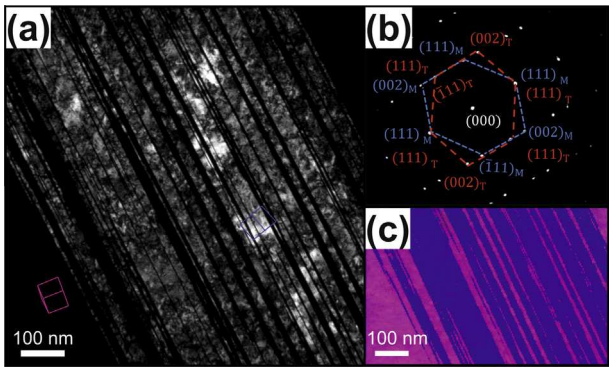

Fig. 5. Deformation twins at ~45% true strain in $Fe_{40}Mn_{40}Co_{10}Cr_{10}$ revealed by TEM: (a) dark field micrograph with beam direction [002]T; (b) selected-area diffraction pattern; (c) orientation and phase mapping of the same area by the ASTAR software.

of the single twins are terminated inside the grains which may be due to two possible reasons: (i) The presence of dislocation loops or dislocations whose Burgers vector is not parallel to the twinning shear direction and which cannot easily cross slip; or (ii) the resolved shear stress in twinning direction falling below the activation shear stress [44]. A further increase in strain to ~25% results in a larger twinning activity, leading to a well-developed twin substructure (Fig. 6c). In some grains the activity of double twin systems was observed, as shown in Fig. 6c_3. Similar double twin systems activation has been observed in brass (15% Zn) after 37% of rolling reduction [45] and in TWIP steels [46].

When analyzing the deformation substructures occurring at higher strains (~25%) using a combination of ECCI and EBSD, the appearance of the two different twinning substructures are found to be related to the grain orientations, as shown in Fig. 7. Two grains with different orientations are shown in Fig. 7a_1 and b_1, the respective orientations relative to the Tensile Direction (TD) are presented in the inserted IPF triangles. The simulated diffraction patterns obtained from EBSD analysis are shown in Figure a_2 and b_2. For grains oriented along ⟨1 1 2⟩//TD, a lamellar twin substructure was observed (Fig. 7a_1). By trace analysis, the twinning plane was found to be (1 −1 1) crystallographic plane. For grains oriented close to ⟨1 1 1⟩//TD, a second twin system was activated with twinning planes (1 −1 1) and (1 1 −1), as shown in Fig. 7b.

The grain orientation dependence of the dislocation and twin substructures in the corresponding deformation levels are summarized in Fig. 8. The average orientation of grains is placed in the TD-IPF figure according to different deformation substructure observed in ECCI. At low deformation levels of ~5% strain, a modest trend is observed regarding grains orientated close to ⟨0 0 1⟩//TA to build up DCs structures, while the majority of the grains developed HDDWs substructures. As the strain increases to about 10%, the same tendency becomes more obvious, namely, the grains with DCs substructures are always orientated near ⟨0 0 1⟩//TD. Besides this observation, the deformation twins are found in some specific grains with orientation ⟨1 1 1⟩//TD. At a strain level of ~25%, the appearance of double twin systems in grains with a particular orientation close to ⟨1 1 1⟩//TD are observed. A single twin system was observed in grains orientated near ⟨1 1 2⟩//TD, and the grains orientated near ⟨0 0 1⟩//TD are mostly found to be free of twins.

4. Discussion

The results presented here demonstrate that a single fcc phase solid solution can be achieved in the four-component FeMnCoCr system, provided that Cr and Co concentrations are lower than strictly equi-atomic fractions. This enables avoiding the Cr-rich σ intermetallic phase that has often been observed in high Cr-containing steels [48] and in many HEA systems with a high amount of Cr [25,26,49]. The instability of Cr in the fcc matrix was described in an ab initio study of the FeNiCoCr alloy [50], where the vacancy formation energy by the removal

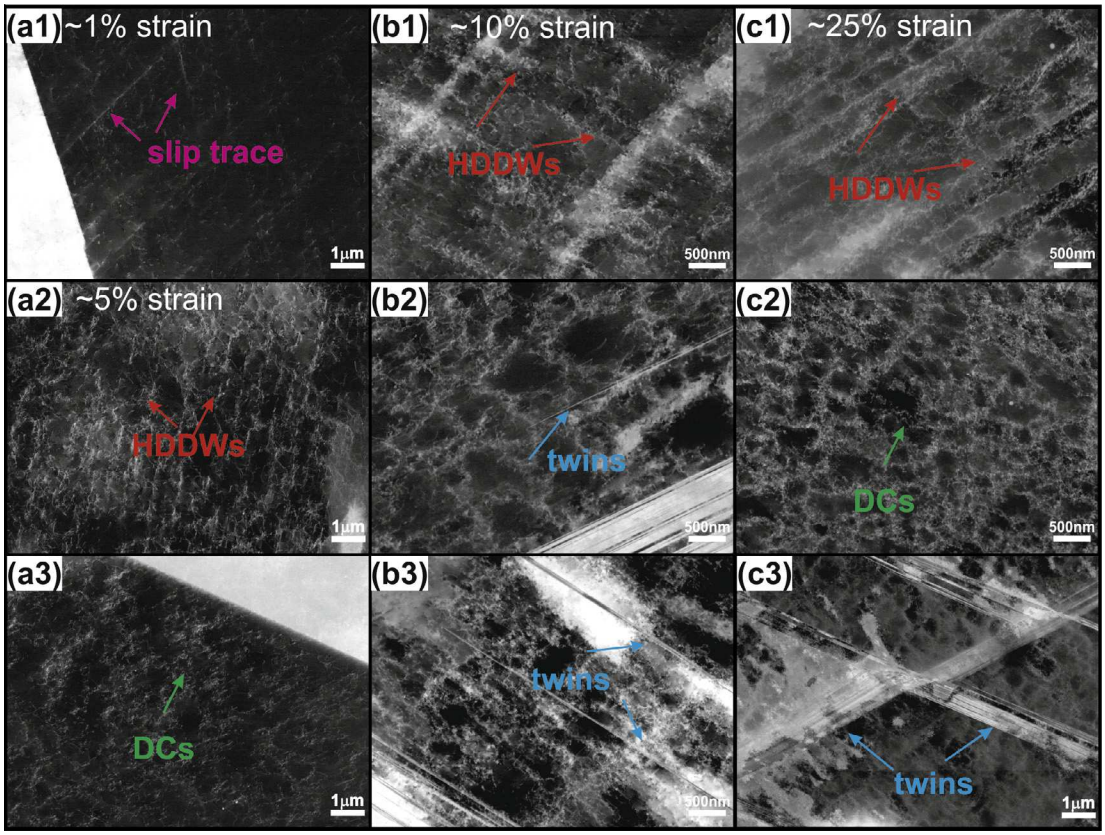

Fig. 6. Deformation microstructure in $Fe_{40}Mn_{40}Co_{10}Cr_{10}$ revealed by ECCI at different strain levels: (a) <5% strain; (b) ~10% strain; (c) ~25% strain.

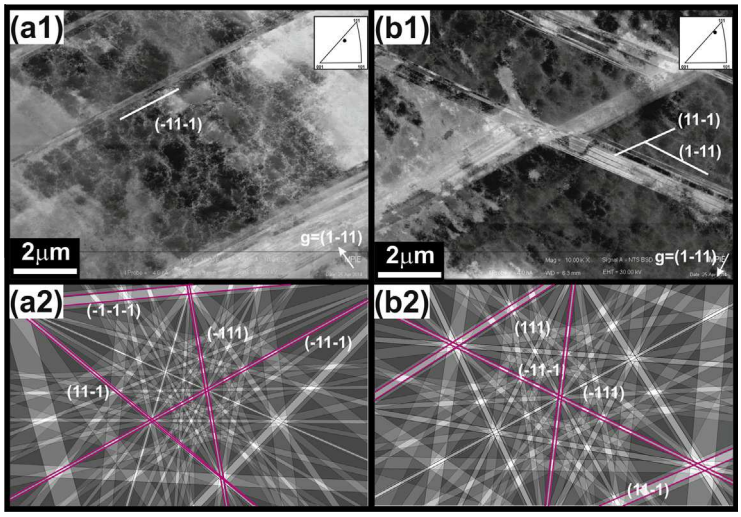

Fig. 7. Trace analysis of the crystallographic orientation of the High Density Dislocation Walls (HDDWs) by using a combination of EBSD and ECCI: (a1) grain containing only one twin system; (b1) grain containing double twin systems; simulated diffraction patterns for each grain (a2) and (b2) using the software TOCA [47].

of Cr is negative while for Fe, Ni and Co it is positive, indicating the inherent precipitation trend of Cr from the FeNiCoCr matrix. Avoiding the σ phase leads to a single fcc phase that resembles the binary Fe–Mn γ phase both crystallographically (lattice parameter = 3.62 Å vs. 3.63 Å [51], respectively) and mechanically [16,17,20,22].

In contrast to most proposed HEA's that lack tensile ductility, the single fcc phase FeMnNiCoCr systems [2,8,13,14] exhibits high ductility and toughness at room temperature as shown in Fig. 9. Thus, the potential for room temperature applications of this system depends on the possibility of enhancing the strength and toughness to

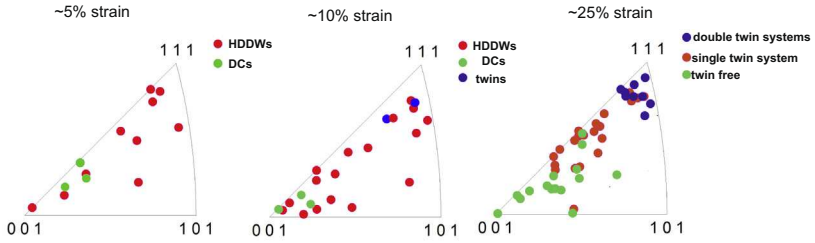

Fig. 8. Orientation dependence of highly dense dislocation walls (HDDWs), dislocation cells (DCs), and twin substructures of $Fe_{40}Mn_{40}Co_{10}Cr_{10}$ at strain levels of ~5%, ~10% and ~25%.

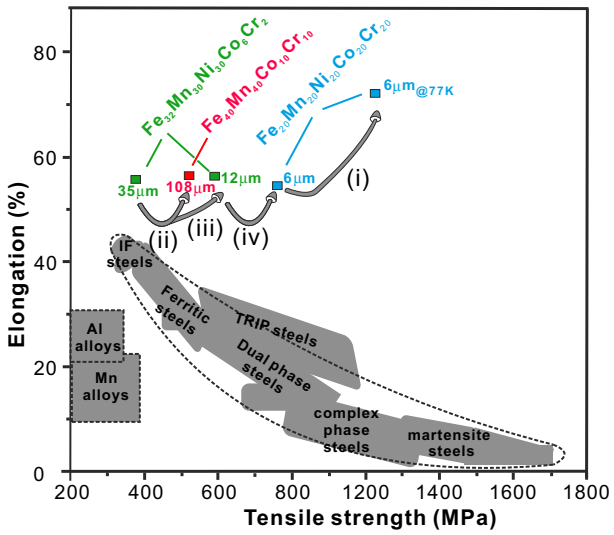

Fig. 9. Strength-ductility properties of different fcc HEAs at room temperature [13,14,52] and at 77 K [18]. Property data of other alloys are reproduced from [53]. Grain size of each tested material is written next to the data points.

levels that justify the extensive amount of alloying (in comparison with respect to, e.g. advanced high strength steels [12,13,16,18]). Based on the results presented here and in related publications the mechanical properties are summarized in Fig. 9, which can be used to understand the contribution of the various strengthening mechanisms.

An essential novelty of the current finding lies in the fact that the newly designed $Fe_{40}Mn_{40}Co_{10}Cr_{10}$ alloy introduced here shows deformation-induced nanotwinning at room temperature. On the other hand the equiatomic $Fe_{20}Mn_{20}Ni_{20}Co_{20}Cr_{20}$ system exhibited deformation twinning only at 77 K [18] (see comparison (i) in Fig. 9). The positive influence of nanotwinning on the tensile strength can be seen when comparing the mechanical properties of the $Fe_{40}Mn_{40}Co_{10}Cr_{10}$ alloy with those of the $Fe_{32}Ni_{30}Mn_{30}Co_6Cr_2$ alloy (see comparison (ii) in Fig. 9) both of which are single phase fcc solid solution alloys. Considering that the grain size of the former is almost one third of the latter, and keeping in mind the strong Hall–Petch effect in these systems (see comparison (iii) in Fig. 9), the improvement in the strength mainly by the activation of nanotwinning is quite significant. It demonstrates that the strength increase and specifically of the strain hardening capacity of the newly developed alloy can be attributed to the reduction in the SFE, i.e. to nanotwinning and the interactions among the partial dislocations. On the other hand, the frictional stress in HEAs is assumed to be high due to the massive lattice distortion caused by the different atomic radii and moduli [54]. The parelastic and dielastic contributions however are dependent on the alloying content. This is seen by comparison of data points (iv) in Fig. 9 for the non-equiatomic $Fe_{32}Ni_{30}Mn_{30}Co_6Cr_2$ system (Sc ~ 11 J/K mol) introduced by the authors [14], and the equiatomic $Fe_{20}Mn_{20}Ni_{20}Co_{20}Cr_{20}$ (Sc ~ 13 J/K mol). Hence, the solid solution strengthening effect does also play a certain role for the measured strength of HEA's.

When focusing more on the deformation mechanisms, a clear transition is seen from prevalent dislocation slip at low strains to slip plus twinning at high strains. At low strain levels (<10%), deformation proceeds mainly by dislocation planar slip (HDDWs), and DCs appear only in grains orientated along ⟨001⟩//TD. At high strain levels, when the true strain is above 25%, an increased twinning activity has been observed with a clear orientation dependence of the formation of the twin substructure [46]. The planar slip in fcc metals is known to be promoted by increasing frictional stress and the decreasing stacking fault energy (SFE), where the latter effect promotes formation of partial dislocations and an increase in the associated constriction and cross slip activation barrier.

From the thermodynamic point of view, a reduction in SFE indicates a reduction of energy difference between the fcc and hcp phases. Furthermore, the Suzuki mechanism [55] is an additional effect to explain the reduction of the SFE in conventional single phase alloys due to solute segregation to stacking faults [56]. However, HEAs lack interstitial atoms, and thus do not experience any long-range diffusion [7] to form Suzuki-type segregation zones. Also, an atomistic relaxation around the SF to relieve the high energy level of the distorted matrix was proposed to also reduce the SFE further [12]. Here, although no direct measurements have been conducted to measure the SFE in the $Fe_{40}Mn_{40}Co_{10}Cr_{10}$ alloy, the appearance of deformation twins at RT suggests a lower SFE of the current alloy compared to the $Fe_{20}Mn_{20}Ni_{20}Co_{20}Cr_{20}$ reference material (25 mJ/m^2) where no deformation twins were observed at room temperature [13,14,18]. Note that also in high Mn steels, the SFE boundary between TRIP and TWIP effects is proposed to be around 20 mJ/m^2 [15].

The formation of DCs is associated with dislocation cross slip and multiple slip [42,43]. Multiple slip can be correlated with the respective Schmid factors. In grains with orientations near ⟨001⟩//TD (seen in Table 1), 8 slip systems are equally stressed, hence they can be activated simultaneously [57,58]. Cross slip enables the possibility of switching to another slip plane. The frequency of screw dislocations moving from one slip plane to another is mainly

Table 1. The Schmid factors of different slip and twin systems with respect to grain orientation.

Slip systems	⟨001⟩//TD		⟨112⟩//TD		⟨111⟩//TD		Twin systems
(111)[1−10]	0	−0.47	0	−0.31	0	0	(111)[11−2]
(111)[10−1]	0.41	0.24	0.3	0.16	0	0	(111)[1−21]
(111)[01−1]	0.41	0.24	0.3	0.16	0	0	(111)[−211]
(1−11)[110]	0	0.24	0.27	0.39	0.27	0.31	(1−11)[121]
(1−11)[011]	0.41	0.24	0.41	−0.08	0.27	−0.16	(1−11)[21−1]
(1−11)[10−1]	0.41	−0.47	0.14	−0.31	0	−0.16	(1−11)[−112]
(11−1)[101]	0	−0.47	0	0	0	0.31	(11−1)[112]
(11−1)[011]	0.41	0.24	0	0	0.27	−0.16	(11−1)[1−2−1]
(11−1)[1−10]	0.41	−0.24	0	0	0.27	0.16	(11−1)[−21−1]
(1−1−1)[110]	0	−0.24	0.3	−0.39	0.3	−0.31	(1−1−1)[211]
(1−1−1)[101]	0.41	0.24	0.41	−0.08	0.3	−0.16	(1−1−1)[12−1]
(1−1−1)[01−1]	0.41	−0.47	0.14	−0.31	0	−0.16	(1−1−1)[1−12]

governed by the activation barrier required for partial dislocation constriction, which in turn depends on the SFE of the alloy. In the present $Fe_{40}Mn_{40}Co_{10}Cr_{10}$ alloy with low SFE, the re-combination of the dissociated partial dislocation is difficult, hence, cross-slip is impeded. Taken into consideration both multiple slip and reduced cross slip, it is plausible that this alloy has a lower frequency of the formation of DCs and the appearance of DCs is concentrated in grains with crystallographic orientation near ⟨001⟩//TD.

The influence of the crystallographic grain orientation on deformation twinning has been investigated previously in terms of the respective Schmid factors for both slip and twinning [46]. Whether deformation twins will be nucleated or not mainly depends on the competition between slip and twinning, which in turn depends on respective Schmid factors of the two deformation mechanisms. For grains orientated along ⟨001⟩//TD, 8 slip systems with higher Schmid factor than those of the twining systems can be activated, and hence deformation is mainly carried by dislocation slip and no deformation twins are observed. For grains with orientations near ⟨112⟩//TD, only the (1−11)[121] twinning system has a comparable high Schmid factor so that both dislocation slip and twinning are activated, as shown in Fig. 7a. In grains near ⟨111⟩//TD, two twinning systems (1−11)[121] and (11−1)[112] can be activated due to their high Schmid factors, Fig. 7b.

5. Conclusions

A non-equiatomic $Fe_{40}Mn_{40}Co_{10}Cr_{10}$ high-entropy alloy was produced by vacuum induction melting, mold casting, hot rolling and homogenization. The microstructure at different processing stages revealed a single homogeneous fcc phase as shown by XRD, EBSD, TEM and APT. The mechanical properties at room temperature were investigated by tensile testing and DIC. To understand the mechanical properties, the deformed substructure at specific strain regions was further revealed by ECCI. The main conclusions are:

(1) In the quaternary FeMnCoCr alloy system, a single phase homogeneous fcc solid solution can be achieved as a non-equiatomic $Fe_{40}Mn_{40}Co_{10}Cr_{10}$ alloy, but not at equiatomic $Fe_{25}Mn_{25}Co_{25}Cr_{25}$ composition.

(2) The mechanical properties of the novel $Fe_{40}Mn_{40}Co_{10}Cr_{10}$ alloy are comparable to those of the FeMnNiCoCr alloy system (except for the occurrence of deformation twinning also at room temperature) and to those of some FeMnC and FeMnAlC TWIP steels.

(3) In this new alloy, at low strains (<10% true strain), deformation is mainly carried by planar dislocation slip; At high strains (>10% true strain), deformation twinning is activated as an additional mechanism, causing a transition in the strain hardening rate similar as in some TWIP steels.

(4) The deformation substructure development in this alloy is strongly grain orientation dependent.

Acknowledgments

The authors would like to thank Dr. Pyuck-Pa Choi, Michael Kulse, Frank Schlüter, Frank Rütters, and Michael Adamek for their contributions. The authors also gratefully acknowledge the funding by the European Research Council under the EU's 7th Framework Programme (FP7/2007-2013)/ERC Grant agreement 290998.

References

[1] J.W. Yeh, S.K. Chen, S.J. Lin, J.Y. Gan, T.S. Chin, T.T. Shun, C.H. Tsau, S.Y. Chang, Nanostructured HEA with multiple principal elements: novel alloy design concepts and outcomes, Adv. Eng. Mater. 6 (2004) 5.

[2] B. Cantor, I.T.H. Chang, P. Knight, A.J.B. Vincent, Microstructural development in equiatomic multicomponent alloys, Mater. Sci. Eng., A 375–377 (2004) 213–218.

[3] B. Cantor, K.B. Kim, P.J. Warren, Novel multicomponent amorphous alloys, Mater. Sci. Forum 386–388 (2002) 27–32.

[4] B. Cantor, Multicomponent and high entropy alloys, Entropy 16 (2014) 4749–4768.

[5] Y. Zhang, T.T. Zuo, Z. Tang, M.C. Gao, K.A. Dahmen, P.K. Liaw, Z.P. Lu, Microstructures and properties of high-entropy alloys, Prog. Mater Sci. 61 (2014) 1–93.

[6] C.C. Tung, J.W. Yeh, T.T. Shun, S.K. Chen, Y.S. Huang, H.S. Chen, On the elemental effect of AlCoCrCuFeNi high-entropy alloy system, Mater. Lett. 61 (2007) 1–5.

[7] C.P. Lee, C.C. Chang, Y.Y. Chen, J.W. Yeh, H.C. Shih, Effect of the aluminium content of $Al_xCrFe_{1.5}MnNi_{0.5}$ high-entropy alloys on the corrosion behaviour in aqueous environments, Corros. Sci. 50 (2008) 2053–2060.

[8] F. Otto, Y. Yang, H. Bei, E.P. George, Relative effects of enthalpy and entropy on the phase stability of equiatomic high-entropy alloys, Acta Mater. 61 (2013) 2628–2638.

[9] D.B. Miracle, High entropy alloys and their development as structural materials, Materials Science and Technology (2015), 1743284714Y.1743284000.

[10] L.J. Santodonato, Y. Zhang, M. Feygenson, C.M. Parish, M.C. Gao, R.J. Weber, J.C. Neuefeind, Z. Tang, P.K. Liaw, Deviation from high-entropy configurations in the atomic distributions of a multi-principal-element alloy, Nat. Commun. 6 (2015) 5964.
[11] K.Y. Tsai, M.H. Tsai, J.W. Yeh, Sluggish diffusion in Co–Cr–Fe–Mn–Ni high-entropy alloys, Acta Mater. 61 (2013) 4887–4897.
[12] P.P. Bhattacharjee, G.D. Sathiaraj, M. Zaid, J.R. Gatti, C. Lee, C.W. Tsai, J.W. Yeh, Microstructure and texture evolution during annealing of equiatomic CoCrFeMnNi high-entropy alloy, J. Alloy. Compd. 587 (2014) 544–552.
[13] F. Otto, A. Dlouhý, C. Somsen, H. Bei, G. Eggeler, E.P. George, The influences of temperature and microstructure on the tensile properties of a CoCrFeMnNi high-entropy alloy, Acta Mater. 61 (2013) 5743–5755.
[14] M.J. Yao, K.G. Pradeep, C.C. Tasan, D. Raabe, A novel, single phase, non-equiatomic FeMnNiCoCr high-entropy alloy with exceptional phase stability and tensile ductility, Scripta Mater. 72–73 (2014) 5–8.
[15] O. Grässel, L. Krüger, G. Frommeyer, L.W. Meyer, High strength Fe–Mn–(Al, Si) TRIP/TWIP steels development — properties — application, Int. J. Plast. 16 (2000) 19.
[16] I. Gutierrez-Urrutia, D. Raabe, Influence of Al content and precipitation state on the mechanical behavior of austenitic high-Mn low-density steels, Scripta Mater. 68 (2013) 343–347.
[17] C.C. Tasan, Y. Deng, K.G. Pradeep, M.J. Yao, H. Springer, D. Raabe, Composition dependence of phase stability, deformation mechanisms, and mechanical properties of the CoCrFeMnNi high-entropy alloy system, JOM 66 (2014) 1993–2001.
[18] B. Gludovatz, A. Hohenwarter, D. Catoor, E.H. Chang, E.P. George, R.O. Ritchie, A fracture-resistant high-entropy alloy for cryogenic applications, Science 345 (2014) 1153–1158.
[19] D.R. Steinmetz, T. Jäpel, B. Wietbrock, P. Eisenlohr, I. Gutierrez-Urrutia, A. Saeed-Akbari, T. Hickel, F. Roters, D. Raabe, Revealing the strain-hardening behavior of twinning-induced plasticity steels: theory, simulations, experiments, Acta Mater. 61 (2013) 494–510.
[20] I. Gutierrez-Urrutia, D. Raabe, Dislocation and twin substructure evolution during strain hardening of an Fe–22wt.% Mn–0.6wt.% C TWIP steel observed by electron channeling contrast imaging, Acta Mater. 59 (2011) 6449–6462.
[21] H. Springer, D. Raabe, Rapid alloy prototyping: compositional and thermo-mechanical high throughput bulk combinatorial design of structural materials based on the example of 30Mn–1.2C–*x*Al triplex steels, Acta Mater. 60 (2012) 4950–4959.
[22] I. Gutierrez-Urrutia, D. Raabe, Multistage strain hardening through dislocation substructure and twinning in a high strength and ductile weight-reduced Fe–Mn–Al–C steel, Acta Mater. 60 (2012) 5791–5802.
[23] A.J. Zaddach, C. Niu, C.C. Koch, D.L. Irving, Mechanical properties and stacking fault energies of NiFeCrCoMn high-entropy alloy, JOM 65 (2013) 1780–1789.
[24] Z. Wu, H. Bei, F. Otto, G.M. Pharr, E.P. George, Recovery, recrystallization, grain growth and phase stability of a family of FCC-structured multi-component equiatomic solid solution alloys, Intermetallics 46 (2014) 131–140.
[25] S. Praveen, B.S. Murty, R.S. Kottada, Phase evolution and densification behavior of nanocrystalline multicomponent high entropy alloys during spark plasma sintering, JOM 65 (2013) 1797–1804.
[26] M.H. Tsai, K.Y. Tsai, C.W. Tsai, C. Lee, C.C. Juan, J.W. Yeh, Criterion for sigma phase formation in Cr- and V-containing high-entropy alloys, Mater. Res. Lett. 1 (2013) 207–212.
[27] B.S. Murty, J.W. Yeh, S. Ranganathan, Intermetallics, interstitial compounds and metallic glasses in high-entropy alloys, in: B.S.M.W.Y. Ranganathan (Ed.), High Entropy Alloys, Butterworth-Heinemann, Boston, 2014, pp. 119–131, Chapter 7.
[28] K.G. Pradeep, N. Wanderka, P. Choi, J. Banhart, B.S. Murty, D. Raabe, Atomic-scale compositional characterization of a nanocrystalline AlCrCuFeNiZn high-entropy alloy using atom probe tomography, Acta Mater. 61 (2013) 4696–4706.
[29] S. Mandal, K.G. Pradeep, S. Zaefferer, D. Raabe, A novel approach to measure grain boundary segregation in bulk polycrystalline materials in dependence of the boundaries' five rotational degrees of freedom, Scripta Mater. 81 (2014) 16–19.
[30] C.C. Tasan, M. Diehl, D. Yan, C. Zambaldi, P. Shanthraj, F. Roters, D. Raabe, Integrated experimental-simulation analysis of stress and strain partitioning in multiphase alloys, Acta Mater. 81 (2014) 386–400.
[31] C.C. Tasan, J.P.M. Hoefnagels, M. Diehl, D. Yan, F. Roters, D. Raabe, Strain localization and damage in dual phase steels investigated by coupled in-situ deformation experiments and crystal plasticity simulations, Int. J. Plast. 63 (2014) 198–210.
[32] Z. Zhao, M. Ramesh, D. Raabe, A.M. Cuitiño, R. Radovitzky, Investigation of three-dimensional aspects of grain-scale plastic surface deformation of an aluminum oligocrystal, Int. J. Plast. 24 (2008) 2278–2297.
[33] I. Gutierrez-Urrutia, S. Zaefferer, D. Raabe, Electron channeling contrast imaging of twins and dislocations in twinning-induced plasticity steels under controlled diffraction conditions in a scanning electron microscope, Scripta Mater. 61 (2009) 737–740.
[34] I. Gutierrez-Urrutia, S. Zaefferer, D. Raabe, Coupling of electron channeling with EBSD: toward the quantitative characterization of deformation structures in the SEM, JOM 65 (2013) 1229–1236.
[35] O. Dmitrieva, D. Ponge, G. Inden, J. Millán, P. Choi, J. Sietsma, D. Raabe, Chemical gradients across phase boundaries between martensite and austenite in steel studied by atom probe tomography and simulation, Acta Mater. 59 (2011) 364–374.
[36] D. Raabe, S. Sandlöbes, J. Millán, D. Ponge, H. Assadi, M. Herbig, P.P. Choi, Segregation engineering enables nanoscale martensite to austenite phase transformation at grain boundaries: a pathway to ductile martensite, Acta Mater. 61 (2013) 6132–6152.
[37] M. Kuzmina, D. Ponge, D. Raabe, Grain boundary segregation engineering and austenite reversion turn embrittlement into toughness: example of a 9wt.% medium Mn steel, Acta Mater. 86 (2015) 182–192.
[38] M.P. Moody, L.T. Stephenson, A.V. Ceguerra, S.P. Ringer, Quantitative binomial distribution analyses of nanoscale like-solute atom clustering and segregation in atom probe tomography data, Microsc. Res. Tech. 71 (2008) 542–550.
[39] N. Mattern, J.H. Han, K.G. Pradeep, K.C. Kim, E.M. Park, D.H. Kim, Y. Yokoyama, D. Raabe, J. Eckert, Structure of rapidly quenched, (Cu0.5Zr0.5)100−xAgx alloys (x = 0–40at.%, J. Alloy. Compd. 607 (2014) 285–290.
[40] D. Raabe, M. Herbig, S. Sandlöbes, Y. Li, D. Tytko, M. Kuzmina, D. Ponge, P.P. Choi, Grain boundary segregation engineering in metallic alloys: a pathway to the design of interfaces, Curr. Opin. Solid State Mater. Sci. 18 (2014) 253–261.
[41] J.W. Christian, S. Mahajan, Deformation twinning, Prog. Mater Sci. 99 (1995) 157.
[42] P. Hähner, A theory of dislocation cell formation based on stochastic dislocation dynamics, Acta Mater. 44 (1996) 8.
[43] N. Hansen, D.A. Hughus, Analysis of large dislocation populations in deformed metals, Phys. Stat. Sol. (b) 149 (1995) 18.
[44] S. Mahajan, Evaluation of slip patterns observed in associated with deformation twins in Mo-35 at% Re alloy, J. Phys. F: Metal. Phys. 2 (1972) 8.
[45] T. Leffers, J.B. Bilde-Sørensen, Intra-and intergranular heterogeneities in the plastic deformation of brass during rolling, Acta Metall. Mater. 38 (1990) 10.

[46] I. Gutierrez-Urrutia, S. Zaefferer, D. Raabe, The effect of grain size and grain orientation on deformation twinning in a Fe–22wt.% Mn–0.6wt.% C TWIP steel, Mater. Sci. Eng., A 527 (2010) 3552–3560.
[47] S. Zaefferer, New developments of computer-aided crystallographic analysis in transmission electron microscopy, J. Appl. Crystallogr. 33 (2000) 10–25.
[48] L.K. Singhal, J.W. Martin, The formation of ferrite and sigma phase in some austenitic stainless steels, Acta Metall. 16 (1968) 11.
[49] M.H. Tsai, H. Yuan, G. Cheng, W. Xu, W.W. Jian, M.H. Chuang, C.C. Juan, A.C. Yeh, S.J. Lin, Y. Zhu, Significant hardening due to the formation of a sigma phase matrix in a high entropy alloy, Intermetallics 33 (2013) 81–86.
[50] S.C. Middleburgh, D.M. King, G.R. Lumpkin, M. Cortie, L. Edwards, Segregation and migration of species in the CrCoFeNi high entropy alloy, J. Alloy. Compd. 599 (2014) 179–182.
[51] M. Ekholm, I.A. Abrikosov, Structural and magnetic ground-state properties of γ-FeMn alloys from ab initio calculations, Phys. Rev. B 84 (2011).
[52] A. Gali, E.P. George, Tensile properties of high- and medium-entropy alloys, Intermetallics 39 (2013) 74–78.
[53] S. Rajasekhara, L.P. Karjalainen, A. Kyröläinen, P.J. Ferreira, Development of stainless steels with superior mechanical properties: a correlation between structure and properties in nanoscale/sub-micron grained austenitic stainless steel (2011) 371–384.
[54] Y. Zou, S. Maiti, W. Steurer, R. Spolenak, Size-dependent plasticity in an $Nb_{25}Mo_{25}Ta_{25}W_{25}$ refractory high-entropy alloy, Acta Mater. 65 (2014) 85–97.
[55] H. Suzuki, Segregation of solute atoms to stacking faults, J. Phys. Soc. Jpn. 17 (1962) 4.
[56] T. Hickel, S. Sandlöbes, R.K.W. Marceau, A. Dick, I. Bleskov, J. Neugebauer, D. Raabe, Impact of nanodiffusion on the stacking fault energy in high-strength steels, Acta Mater. 75 (2014) 147–155.
[57] U.F. Kocks, Polyslip in polycrystals, Acta Matall. 6 (1958) 10.
[58] D. Raabe, P. Klose, B. Engl, K.P. Imlau, F. Friedel, F. Roters, Concepts for integrating plastic anisotropy into metal forming simulations, Adv. Eng. Mater. 4 (2002) 12.